B_r at the CMB, 1995

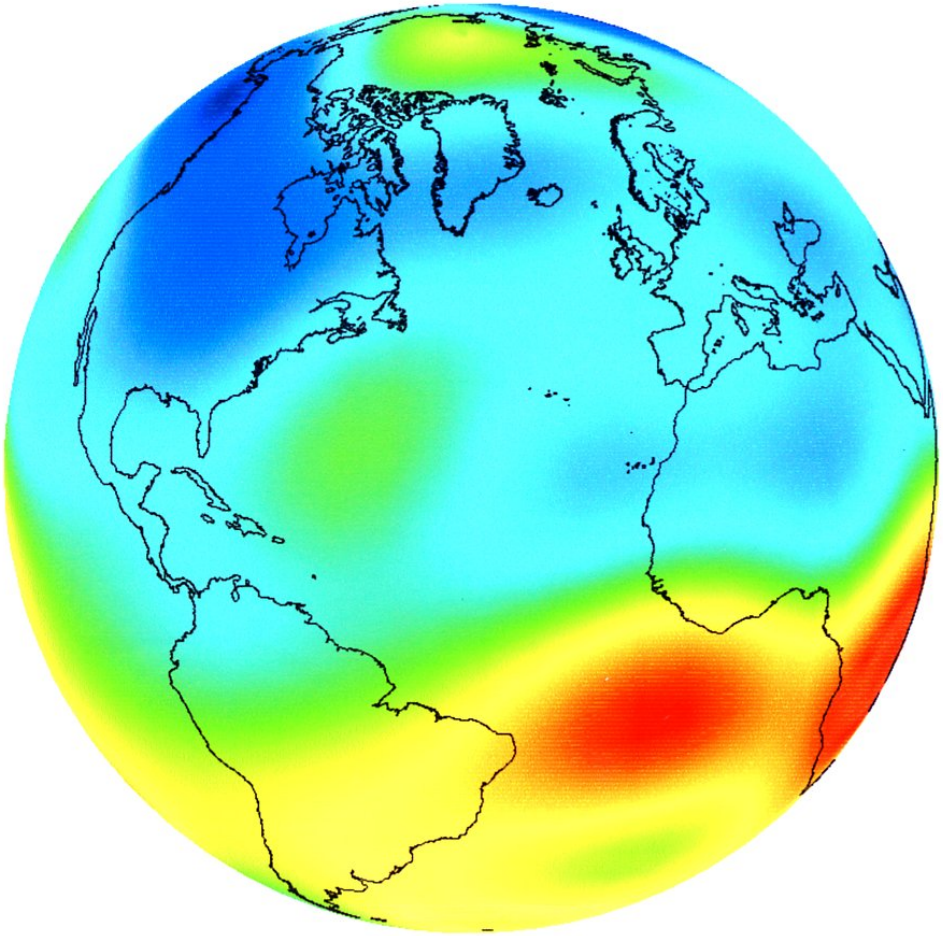

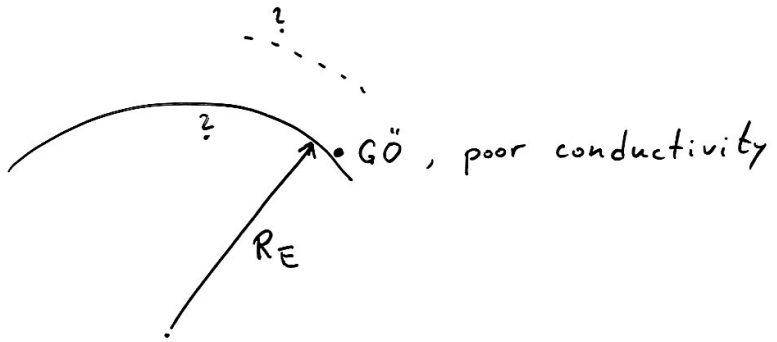

in vacuum:

$$\vec{j} = \frac{1}{\mu_0} \nabla \times \vec{B} = 0 \quad \Rightarrow \vec{B} = \nabla \phi \quad \Rightarrow \nabla^2 \phi = 0$$
$$\nabla \cdot \vec{B} = 0$$

General solution of $\nabla^2 \phi = 0$ in spherical coordinates:

$$\phi(r,\theta,\varphi) = \sum_{l=0}^{\infty} \sum_{m=-l}^{l} Y_l^m(\theta,\varphi) \left[A_{lm} r^l + B_{lm} r^{-(l+1)} \right]$$

$A_{lm} r^l \to \infty$ for $r \to \infty$: Contribution from external sources

$B_{lm} r^{-(l+1)} \to \infty$ for $r \to 0$: Contribution from internal sources

Components of $\vec{B}$ at $r = R_E$:

$$B_\theta = \frac{1}{r}\frac{\partial \phi}{\partial \theta}\Big|_{r=R_E} = \sum\sum \frac{\partial Y_\ell^m}{\partial \theta}\left[A_{\ell m} R_E^{\ell-1} + B_{\ell m} R_E^{-\ell-2}\right]$$

$$B_\varphi = -\frac{1}{r\sin\theta}\frac{\partial \phi}{\partial \varphi}\Big|_{r=R_E} = \sum\sum -\frac{1}{\sin\theta}\frac{\partial Y_\ell^m}{\partial \varphi}\left[A_{\ell m} R_E^{\ell-1} + B_{\ell m} R_E^{-\ell-2}\right]$$

$$B_r = \frac{\partial \phi}{\partial r}\Big|_{r=R_E} = \sum\sum Y_\ell^m \left[\ell A_{\ell m} R_E^{\ell-1} - (\ell+1) B_{\ell m} R_E^{-\ell-2}\right]$$

1. Get a global map of B_r, B_θ, B_φ
2. From the dependence on θ, φ determine

$$A_{\ell m} R_E^{\ell-1} + B_{\ell m} R_E^{-\ell-2} \quad \text{and}$$

$$\ell A_{\ell m} R_E^{\ell-1} - (\ell+1) B_{\ell m} R_E^{-\ell-2}$$

→ for every ℓ, m there are 2 equations for the 2 unknowns $A_{\ell m}$, $B_{\ell m}$

3. Determine $A_{\ell m}$, $B_{\ell m}$

Largest contributions: B_{10}, B_{11}, $B_{1,-1}$

External sources contribute only a few %

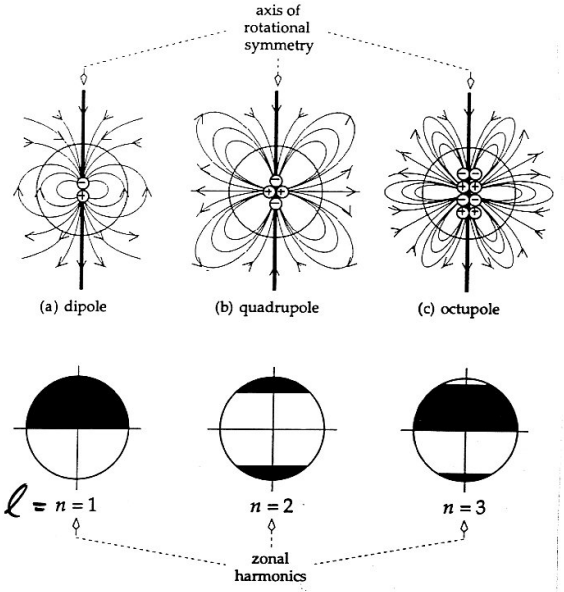

Fig. 5.32 Axial cross-sections showing the field-line geometries of (a) dipole, (b) quadrupole and (c) octupole fields; each field is rotationally symmetrical about the axis of the configuration. The corresponding zonal spherical harmonics are illustrated symbolically by shading the alternate zones in which magnetic field lines leave or return to the surface of a sphere.

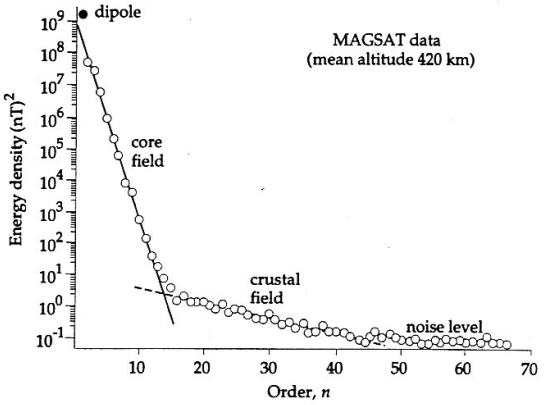

Fig. 5.33 The energy density spectrum derived from measurements of the geomagnetic field made by the MAGSAT Earth-orbiting satellite (after Cain, 1989).

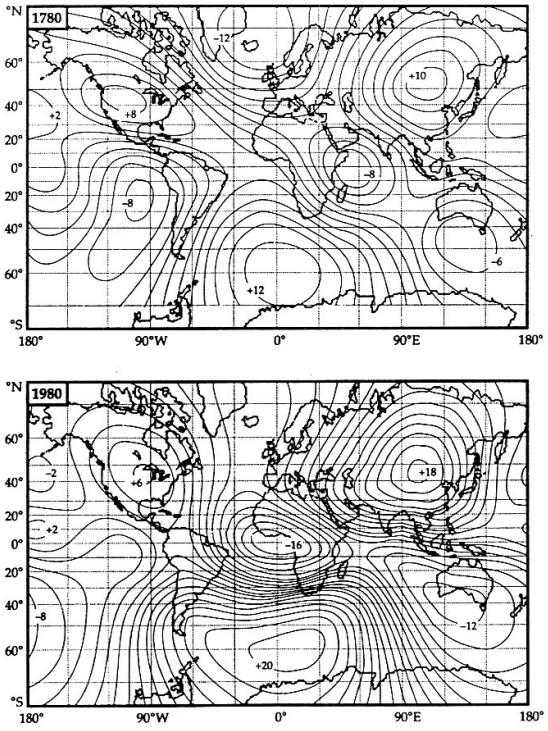

Fig. 5.35 The non-dipole magnetic field for the years 1780 A.D. (after Yukutake and Tachinaka, 1968) and 1980 A.D. (after Barton, 1989).

~5% of the total field

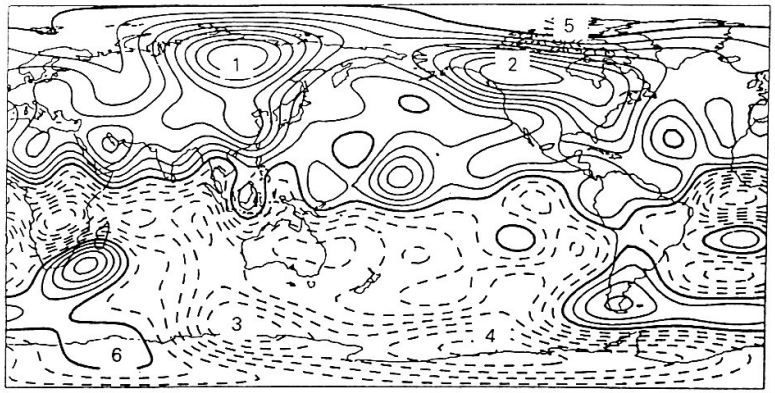

Figure 5.8 Map of the radial component of the magnetic field at the CMB for 1980. Contour interval is 100 μT; solid contours represent flux into the core, broken contours flux out of the core; bold contours represent zero radial field. The two main pairs of lobes (1,3) and (2,4) are indicated, as are the patches of low radial field (5 and 6) near the poles (after Gubbins and Bloxham, 1987).

1. Determine A_{lm} and B_{lm} at $r = R_E$
2. Assume the mantle is insulating
3. Compute $\vec{B}$ at $r = R_{CMB}$ from $B = \nabla\phi$ and

$$\phi = \sum_l \sum_m Y_l^m(\theta,\varphi)\left[A_{lm} r^l + B_{lm} r^{-(l+1)}\right]$$

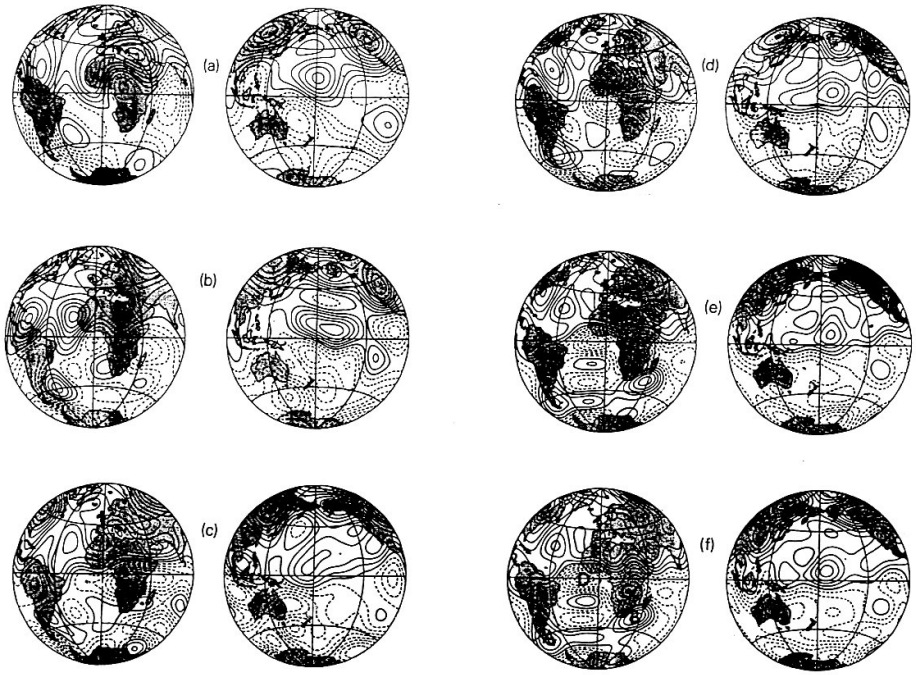

Figure 5.7 Contour plots of the radial field at the CMB for (a) 1715.0; (b) 1777.5; (c) 1842.5; (d) 1905.5; (e) 1969.5; and (f) 1980.0. The contour interval is 100 μT; solid contours represent flux into the core, broken contours flux out of the core. The bold contours represent zero radial field (after Bloxham and Gubbins, 1985).

1. static flux bundles (Arctic Canada, Siberia, Antarctica, Central Pacific Ocean)

2. rapidly drifting flux spots (Africa)
   → westward drift

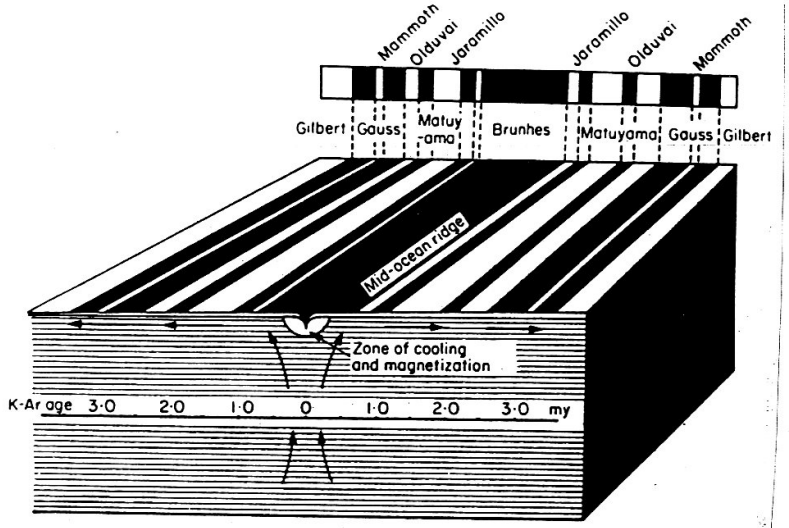

Fig. 5.5. Schematic representation of sea-floor spreading and the formation of linear magnetic anomalies due to reversals of the Earth's magnetic field. Normal polarity zones are shaded.

+ lava flows

+ sediments

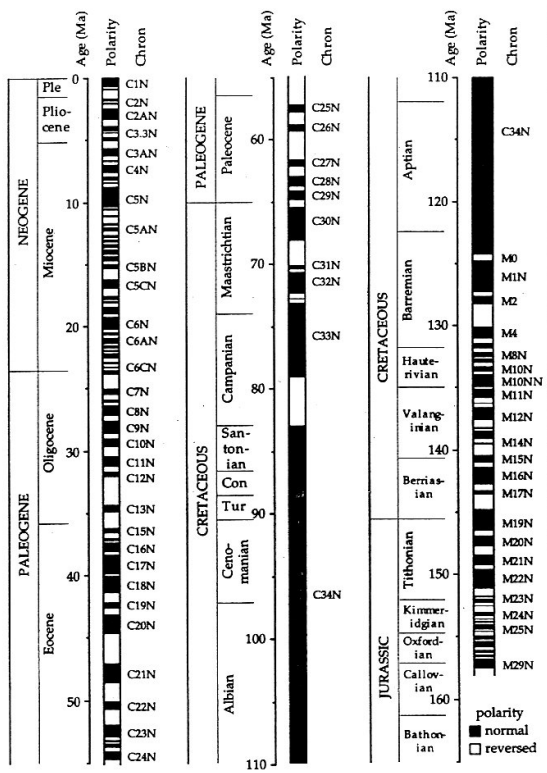

Fig. 5.78 The geomagnetic polarity timescale since the late Jurassic (based upon Harland *et al.*, 1990). Designations for normal polarity chrons are listed.

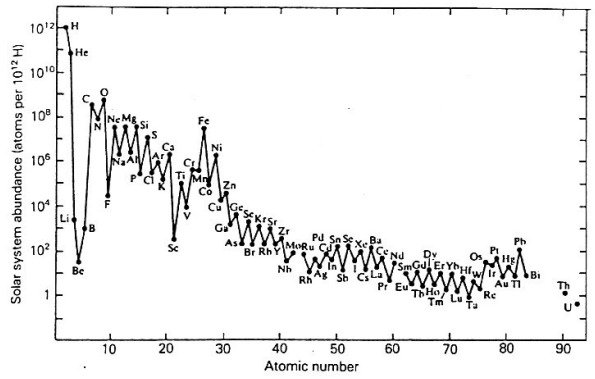

Figure 3.6 Solar system abundances of the elements, showing the relative number of atoms present on a logarithmic scale, normalized to the value 10^{12} for H (based on a combination of solar spectrum and meteorite data) (after Cox, 1989).

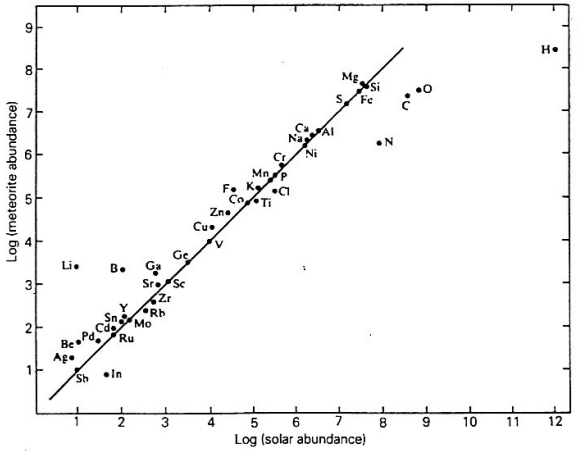

Figure 3.7 Comparison between abundances of elements with atomic numbers between 1 and 51 found in carbonaceous chondrite meteorites, with those in the sun (after Cox, 1989).

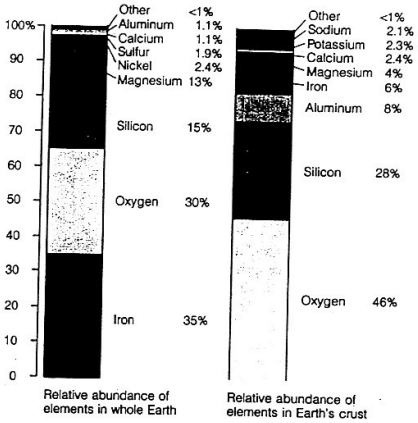

Figure 1-12
Relative abundance by weight of elements in the whole Earth and in the Earth's crust. Differentiation has resulted in a light crust depleted in iron and enriched in oxygen, silicon, aluminum, calcium, potassium, and sodium.

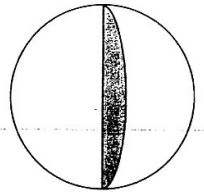

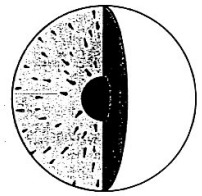

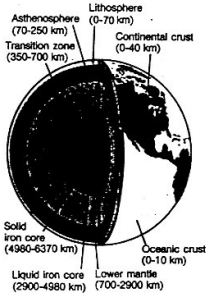

Figure 1-10
The early Earth (top) was probably a homogeneous mixture, with no continents or oceans. In the process of differentiation, iron sank to the center and light material floated upward to form a crust (middle). As a result, the Earth is a zoned planet (bottom), with a dense iron core, a surficial crust of light rock, and, between them, a residual mantle.

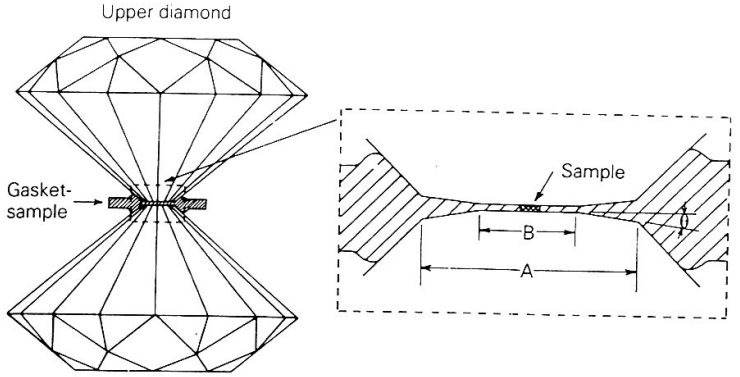

Figure 3.1 Sketch of the diamond-anvil pressure cell. Distance from the top surface of upper diamond to bottom surface of lower diamond ~5 mm. Inset – magnified view of a cross-section of the gasket-sample assembly. The sample width is 250 μm (after Mao and Bell, 1978).

Heat the sample with a laser
- Diamond cannot withstand high temperatures
→ Temperature inhomogeneities in the sample

Problems with diagnostics

Alternative: shock waves

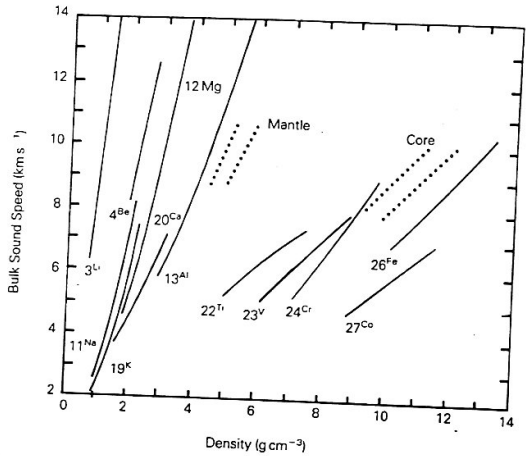

Figure 3.3 Bulk sound speed

$$\left(\frac{\partial p}{\partial \rho}\right)_s^{1/2}$$

versus density for a number of elements along the Hugoniot compression curves. Atomic numbers are attached to each curve. The areas in which the corresponding quantities for the Earth's mantle and core must lie are indicated by the pairs of dotted lines (after Birch, 1968).

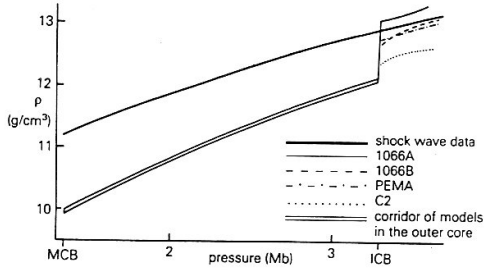

Figure 3.4 Density models of the core compared with shock wave data for iron (after Jacobs, 1980).

Unwary readers should take warning that ordinary language undergoes modification to a high pressure form when applied to the interior of the Earth: a few examples of equivalents follow:

High pressure form	*Ordinary meaning*
certain	dubious
undoubtedly	perhaps
positive proof	vague suggestion
unanswerable argument	trivial objection
pure iron	uncertain mixture of all the elements.

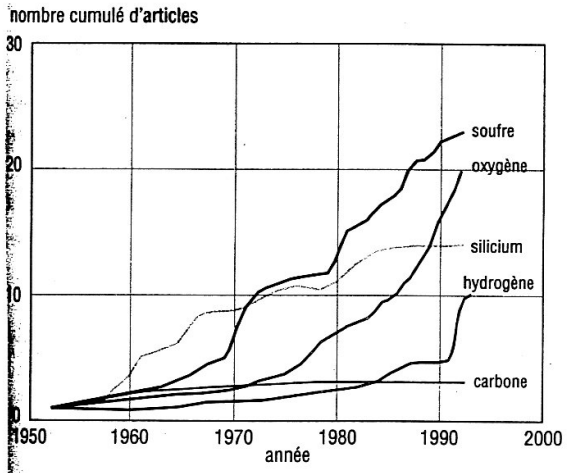

nels éléments légers
ns le noyau ?
on analyse,
fonction du temps,
nombre cumulé d'articles
ns les journaux spécialisés
ont apporté des arguments
en faveur des différents
éléments légers,
on s'aperçoit que
certains éléments
ont été plus « populaires »
que d'autres à certaines époques.
Y a-t-il un effet de mode ?

Fig. 2. The state of our five bodies in Figure 1 at some later time that is different for each body. Each of the bodies has differentiated to form an iron or iron alloy core. The largest body will differentiate most quickly. The size of the core will depend on the initial composition of the body and the degree to which differentiation takes place. Since the Moon is believed to have assembled from iron poor material, its core should be relatively smaller than the others.

because of stronger gravity

Fig. 3. A later stage of the thermal evolution of the bodies in Figure 2. The bodies now have cooled to the point that their inner cores have begun to solidify. We expect this cooling to occur most rapidly on the smallest bodies while core formation itself should occur most rapidly for larger bodies. Additional heat sources such as tidal forces and radioactivity could slow the cooling process.

Table 5.2 *Magnetic characteristics of the planets (data from Russell, 1980).*

PLANET	Mean orbital radius (AU)	Mean radius of planet (km)	Period of rotation (days)	Magnetic dipole moment (m_E)	Equivalent equatorial magnetic field (nT)	Dipole tilt to rotation axis (°)
Mercury	0.387	2440	58.6	$(2–7)\times10^{-4}$	100–400	—
Venus	0.723	6051	243.7	$<10^{-5}$	<1	—
Earth	1	6371	1	1	30,400	11.4
Moon	0.00257	1738	27.3	—	—	—
Mars	1.524	3370	1.029	$(1–30)\times10^{-5}$	2–60	(15–20)?
Jupiter	5.203	69,910	0.415	19,400	450,000	9.7
Saturn	9.539	58,230	0.445	575	23,000	<1
Uranus	19.18	25,460	0.718	50	24,000	60

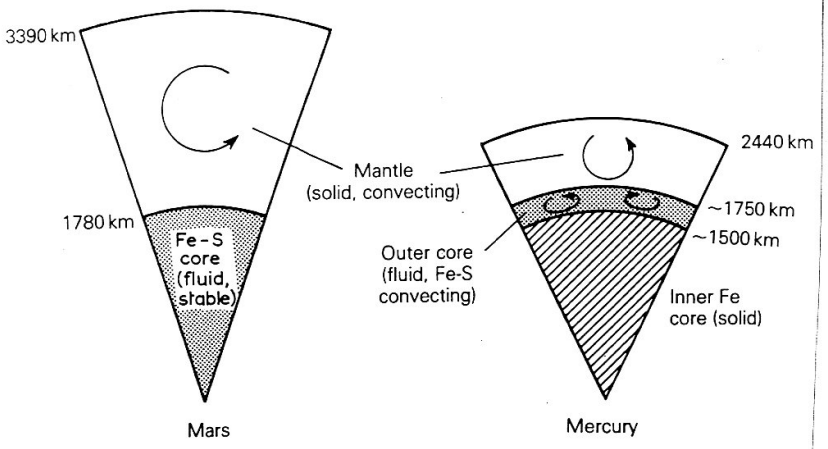

Figure 7.1 Schematic representation of probable present-day states for Mars and Mercury. Mars may have no IC if the core is sulphur-rich whereas Mercury's core may be mostly frozen because of very low sulphur abundance. The thin but vigorously convecting Mercurian fluid shell may be capable of magnetic field generation (after Stevenson, 1983).

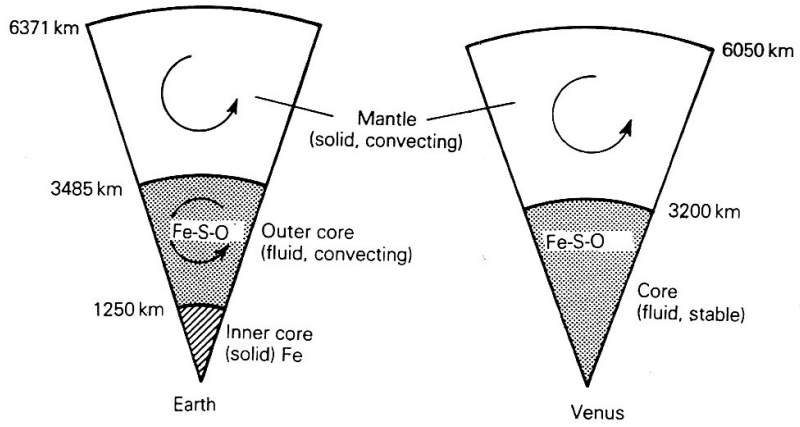

Figure 7.2 Schematic representation of probable present-day states for Earth and Venus. The lower pressures and higher temperatures in Venus may prevent IC growth. This would cause the core to be stably stratified and incapable of magnetic field generation (after Stevenson, 1983).

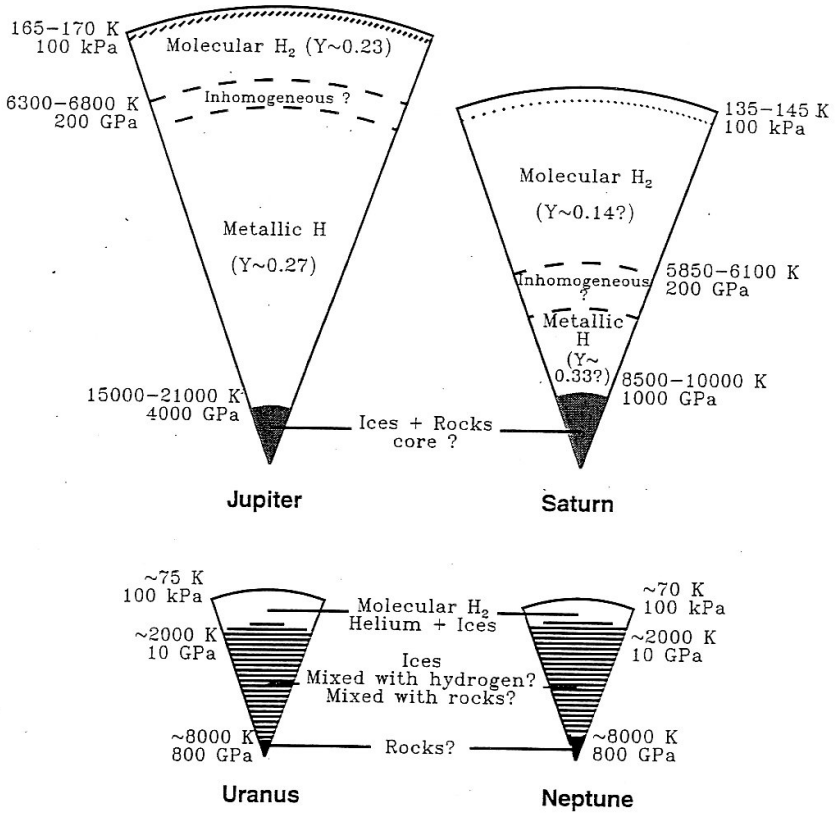

Guillot. Science 286. 72. 1999.

Convection:

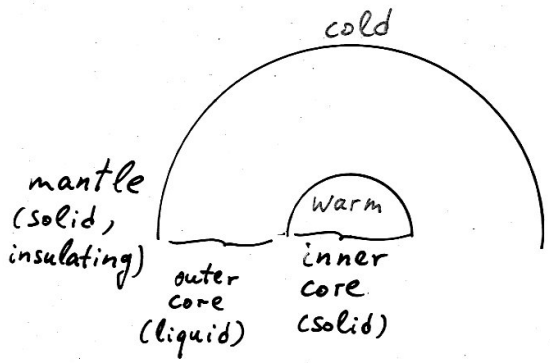

- Remanent heat from the formation of the earth
- Radioactive decay
- Heat of crystallization
- Compositional differences

Temperature gradient needs to be "superadiabatic"

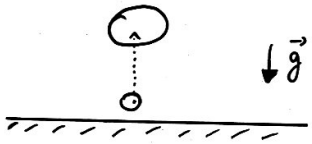

Precession:

Tidal forcing

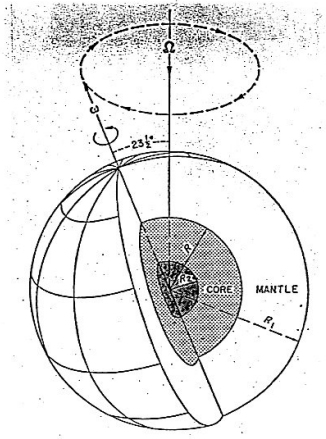

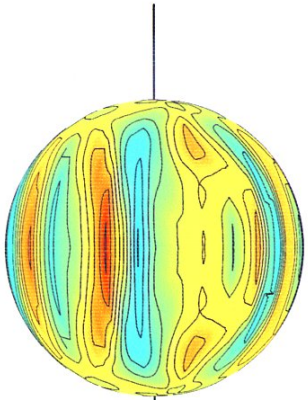

v_r

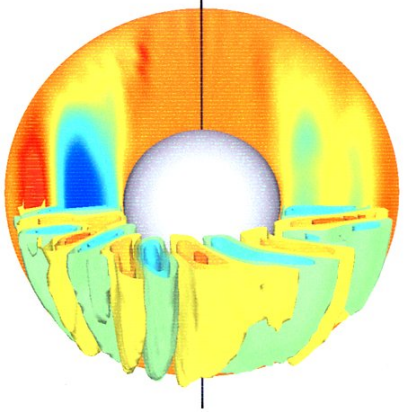

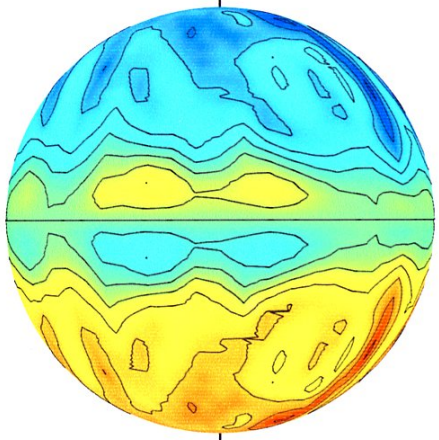

B_r

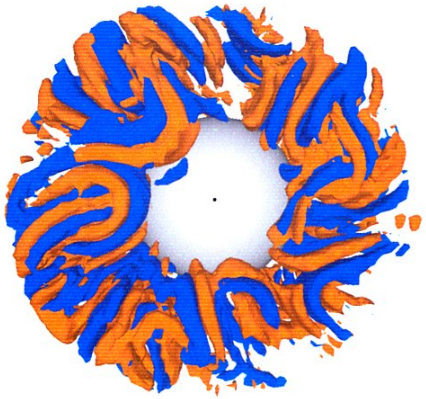

j_r

$Ra = 4.5 \cdot 10^5$

$E = 2 \cdot 10^{-4}$

$Pr = 1$

$Pm = 6$